Chemical Engineering Journal 396 (2020) 125315

Contents lists available at ScienceDirect

Chemical Engineering Journal

journal homepage: www.elsevier.com/locate/cej

Iron doped Ni_3S_2 nanorods directly grown on $FeNi_3$ foam as an efficient bifunctional catalyst for overall water splitting

Wenxiu Zhang[a], Qiang Jia[a], Hui Liang[a], Liang Cui[b,*], Di Wei[b], Jingquan Liu[a,b,*]

[a] *College of Materials Science and Engineering, Institute for Graphene Applied Technology Innovation, Qingdao University, Qingdao 266071, China*
[b] *College of Materials Science and Engineering, Linyi University, Linyi 276000, Shandong, China*

HIGHLIGHTS

- Fe-doped Ni_3S_2 nanorods are synthesized by a simple one-step hydrothermal method.
- Application of bimetallic composite foam ($FeNi_3$) avoid the use of iron salt reagents.
- Fe doping significantly improves the catalytic performance of Ni_3S_2.
- Fe-Ni_3S_2@$FeNi_3$-8 can achieve efficient overall water splitting and urea electrolysis.

GRAPHICAL ABSTRACT

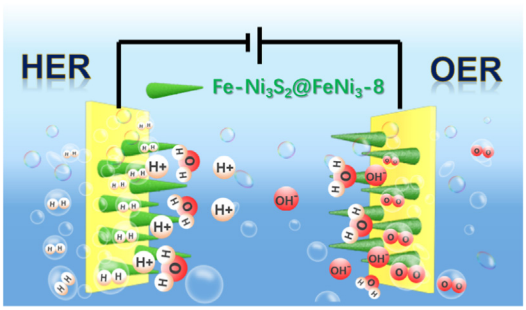

ARTICLE INFO

Keywords:
One-step hydrothermal method
Hydrogen evolution reaction
Oxygen evolution reaction
Overall water splitting
Urea oxidation reaction

ABSTRACT

The development of high-performance and inexpensive bifunctional electrocatalysts to replace precious metal catalysts for hydrogen evolution reaction (HER) and oxygen evolution reaction (OER) remains a thorny issue in the field of electrochemical water splitting. Here, a three-dimensional rods array catalysts of Ni_3S_2 doped with trace amount of Fe on foam $FeNi_3$ (Fe-Ni_3S_2@$FeNi_3$) are synthesized. It is found experimentally that Fe-Ni_3S_2@$FeNi_3$ has excellent catalytic activity and corrosion resistance in both acidic, neutral and alkaline solutions. In 1.0 M KOH solution, only small overpotentials of 105 mV and 213 mV are required to achieve the current densities of 10 mA cm^{-2} for HER and OER respectively. In addition, Fe-Ni_3S_2@$FeNi_3$-8 also exhibits excellent catalytic activity in 0.5 M H_2SO_4 solution (η_{10} = 48 mV) and 1.0 M PBS solution (η_{10} = 83 mV) for HER. In 1.0 M KOH and 0.33 M urea solution, Fe-Ni_3S_2@$FeNi_3$-8 requires only 1.40 V to provide the current density of 10 mA cm^{-2} for urea oxidation reaction (UOR). As evidenced, doping Fe element into catalyst can significantly increase the catalytic activities for HER and OER. This work demonstrates a new and facile approach to prepare novel bimetallic transition metal catalysts as inexpensive alternatives to precious metal catalysts for efficient hydrogen production.

1. Introduction

Global climate change is a very serious problem that has received widespread attention from the international community. Therefore, how humans protect the ecological environment while develop and use energy has become a global issue. The large amount of greenhouse gas emission caused by the excessive development and utilization of fossil energy has become the main cause of global warming [1]. Therefore,

---

[*] Corresponding authors at: College of Materials Science and Engineering, Linyi University, Linyi 276000, Shandong, China (L. Cui). College of Materials Science and Engineering, Institute for Graphene Applied Technology Innovation, Qingdao University, Qingdao 266071, China (J. Liu).

E-mail addresses: cuiliang@lyu.edu.cn (L. Cui), weidi-cnc@pku.edu.cn (D. Wei), jliu@qdu.edu.cn (J. Liu).

https://doi.org/10.1016/j.cej.2020.125315
Received 1 February 2020; Received in revised form 10 April 2020; Accepted 30 April 2020

limiting and reducing greenhouse gas emissions have become an important issue to mitigate global climate change. Therefore, from the perspective of the evolution of the energy landscape, the replacement of traditional energy sources with new clean energy is the general trend. Zero carbon content hydrogen is a very popular source of energy [2,3]. The product after hydrogen combustion is water, and water can produce hydrogen by electrochemical water splitting, so hydrogen is absolutely a renewable energy source and in line with our demand for clean energy [4,5]. To date, the amount of hydrogen produced by electrochemical water splitting has accounted for only 4% of global production, which is mainly due to the fact that electrochemical water splitting requires sufficient potential to drive the progress of HER and OER. Thus it is necessary to find a highly efficient catalyst to reduce the overpotential. At present, the most efficient catalysts for HER and OER are Pt-, Ir- and Ru-based catalysts. However, due to the scarcity and high cost of these precious metals, their large-scale application is severely limited [6,7]. Therefore, it is an inevitable trend to find inexpensive and highly efficient non-precious-metal catalysts.

Compared with precious metals, the crustal reserves of transition metals are much richer, therefore they are low cost. Moreover their compounds are even more stable in electrolyte solution. Therefore, transition metals have become a research hotspot in recent years, for example, transition metal sulfides [8–16], phosphides [17–19], selenides [20,21], oxides [22–26], hydroxides [27,28]. In addition, the perovskite catalyst also shows excellent catalytic performance [29]. Among them, nickel sulfide catalysts have great development prospects. Ren et al. synthesized Ni_3S_4 nanosheets (NiS/NF) on nickel foam by hydrothermal-vulcanization method. For HER under alkaline condition of 1.0 M KOH, only the overpotential of 122 mV was required when the current density reached 10 mA cm^{-2}. While for OER, only an overpotential of 122 mV was required to achieve a current density of 20 mA cm^{-2} [30]. Ma et al. synthesized NiS_2 (NiS_2/NF) on foamed nickel, which only required an overpotential of 122 mV to reach a current density of 10 mA cm^{-2} in 1.0 KOH solution for HER [31]. In addition, the combination of nickel sulfides with other elements is an effective way to improve the performance of catalysts. Zhang et al. synthesized a MoS_2/Ni_3S_2 heterostructure on foamed nickel by a hydrothermal method as a high-efficient catalyst for OER. Only an overpotential of 218 mV was required to achieve a current density of 10 mA cm^{-2} in 1.0 M KOH solution [32]. Yan et al. reported the preparation of Fe-doped NiS_2 (Fe-NiS_2) nanosheets as a high-performance catalyst for HER. Their studies revealed that that the successful doping of Fe^{3+} into the surface lattice of the (0 0 2) plane of NiS_2 could reduce the activation energy for generating H_2 [33]. Recent studies have also shown that such 3D structure (such as, Ni foam and $FeNi_3$ foam) as a carrier is helpful to enhance the performance of the catalyst [14,34–36]. In addition, many other studies have also shown that the incorporation of iron ions could significantly improve the performance of catalysts [37,38]. Although the incorporation of iron ions has made a great contribution to the improvement of performance, the preparation process is relatively complicated, and involves more reagents that require after-treatment with high cost and environmental pollutions. Therefore, there is a need for a convenient method to develop high performance catalysts while reducing the environmental protection pressure. In previous reports, Zou et al. [39] and Pan et al. [40] have fabricated Ni_3S_2 on Ni foam via a one-step hydrothermal method. The difference is that we choose $FeNi_3$ foam as the substrate and raw material. Thus, the Fe and Ni elements in the $FeNi_3$ foam can be directly used as the source of Fe and Ni in the catalyst preparation to synthesize Fe-doped Ni_3S_2.

In addition, to find more efficient and inexpensive catalysts to reduce the energy required to produce hydrogen, molecules that can be easily oxidized at the anode (eg, ethanol, hydrazine, urea) can be substituted for OER to achieve more efficient systems for producing hydrogen [41,42]. Among them, urea can be oxidized into non-toxic CO_2 and N_2 via the following reaction equation: $CO(NH_2)_2 + 6OH^- \rightarrow N_2 + 5H_2O + CO_2 + 6e^-$. The main advantage of replacing OER with UOR is that the equilibrium potential of UOR is 0.37 V, which is much smaller than the 1.23 V required by OER [43]. Therefore, when using a two-electrode system to produce hydrogen, urea oxidation reaction (UOR) is an ideal alternative to OER. In addition, the main component of eutrophic wastewater is urea [44-46], so UOR is promising for the treatment of eutrophic wastewater and low-energy production of hydrogen ($CO(NH_2)_2 + H_2O \rightarrow N_2 + 3H_2 + CO_2$).

Herein, based on the above two aspects, we report the preparation of a robust Fe-doped rod-shaped Ni_3S_2 array grown on $FeNi_3$ foam (Fe-Ni_3S_2@$FeNi_3$) as a high-performance bifunctional catalyst by one-step hydrothermal method. The rod-shaped Fe-Ni_3S_2 is strongly anchored on the three-dimensional $FeNi_3$ skeleton to form a 3D network structure, which is beneficial for rapid electron transport. At the same time, the strong 3D rods array not only provides a large number of active sites and a large active surface area, but also makes the structure of the catalyst not easy to collapse, to allow Fe-Ni_3S_2 have the excellent stability. The Fe-Ni_3S_2@$FeNi_3$ can be directly used as an electrode without the binder, which exhibits excellent catalytic activity in 1.0 M KOH alkaline electrolyte. For HER, an overpotential of only 105 mV is required to achieve the current density of 10 mA cm^{-2}. Fe-Ni_3S_2 also has good performance in acidic electrolyte of 0.5 M H_2SO_4 and neutral electrolyte of 1.0 M PBS. For OER, an overpotential of only 213 mV is required to achieve the current density of 10 mA cm^{-2}. In addition, when 0.33 M urea solution is added to a 1.0 M KOH solution, the electrolysis efficiency can be greatly improved. A potential of only 1.40 V is required to achieve the current density of 10 mA cm^{-2} for UOR. When Fe-Ni_3S_2@$FeNi_3$ is used as anode and cathode for the overall water splitting and whole urea electrolysis, only the potentials of 1.59 V and 1.50 V are required to provide the current density of 10 mA cm^{-2}, respectively.

2. Experimental

2.1. Materials

$FeNi_3$ foam was purchased from Suzhou Taili Foam Metal Factory. Anhydrous ethanol, thioacetamide (TAA), urea and ammonium fluoride (NH_4F) were purchased from Sinopharm Chemical Reagent Co., Ltd. Deionized water is obtained from the Flom ultrapure water system. All chemicals are of analytical grade and used without further purification.

2.2. Preparation of the cleaned $FeNi_3$ foam

$FeNi_3$ foam (0.5 × 3 cm^2) was washed four times with deionized water and ethanol for 15 min each time, and then dry in an oven at 60 °C to ensure that the surface of $FeNi_3$ foam is clean enough for later use.

2.3. Synthesis of Fe-Ni_3S_2

4 mmol of thioacetamide (TAA), 9 mmol of urea and 4 mmol of ammonium fluoride (NH_4F) were dissolved in 30 ml of deionized water and sonicated for 5 min to obtain a clear and transparent solution. The solution was then transferred to 50 ml Teflon-lined stainless-steel autoclave, followed by the placement of a clean foam of $FeNi_3$ (0.5 × 3.0 cm). The whole setup was then placed in an electric oven and heated to 120 °C for 8 h, followed by natural cooling to room temperature. After that, the sample was taken out, washed three times with deionized water and absolute ethanol, and then placed in an oven at 60 °C for 5 min to obtain Fe-Ni_3S_2@$FeNi_3$-8. The mechanism is that the raw materials will firstly react with each other to form H^+ in the solution under high temperature and high pressure, and then the $FeNi_3$ foam will be corroded to generate Ni^{2+} and Fe^{2+}. Finally, a large amount of Ni^{2+} and a small amount of Fe^{2+} will react with HS^- to form Fe-doped nickel sulfides (Fe-Ni_3S_2@$FeNi_3$). Similar reaction

mechanisms have been reported before [47].

For experimental comparison, two samples were prepared under the same condition but with different reaction times of 4 h and 12 h. The obtained samples were named as Fe-Ni_3S_2@$FeNi_3$-4, Fe-Ni_3S_2@$FeNi_3$-12, respectively. The exact surface loadings of Fe-Ni_3S_2@$FeNi_3$- (4, 8, 12) were calculated to be 0.79 mg cm^{-2}, 0.82 mg cm^{-2} and 0.87 mg cm^{-2}, respectively.

2.4. Synthesis of Ni_3S_2 and $Fe(OH)_3$

The same method was used to clean the Ni foam and Fe foam. The synthesis of Ni_3S_2 and $Fe(OH)_3$ is similar to that of Fe-Ni_3S_2@$FeNi_3$-8. $FeNi_3$ foam was replaced with Ni foam to prepare Ni_3S_2, and $FeNi_3$ foam was replaced with Fe foam to prepare $Fe(OH)_3$. The exact surface loading of Ni_3S_2 and $Fe(OH)_3$ were calculated to be 0.83 mg cm^{-2} and 0.80 mg cm^{-2}, respectively.

2.5. Characterizations

The surface morphology of the synthesized sample was characterized by scanning electron microscopy (SEM, ZEISS Supra 55) at an accelerating voltage of 10 kV. Transmission electron microscopy images (TEM, JEOL JEM-2010) of the synthesized samples were collected on a JEOL JEM-2010 microscope. The compositions of the synthesized samples were specifically analyzed by high resolution transmission electron microscopy (HRTEM). Selected area electron diffraction (SAED) analysis of the sample was performed at 200 kV on a FEI-Tecnai F20 transmission electron microscope. The phase composition analysis of the synthesized samples was carried out on a Bruker D8 advanced X-ray powder diffractometer with Cu Ka radiation (λ = 1.54056 Å). The analysis of the specific elemental composition of the synthesized sample was carried out by X-ray photoelectron spectroscopy (XPS) on a Thermo ESCALAB 250 using a single-color Al Ka X-ray as the excitation source. The specific element content of the samples was measured on an Agilent 720ES inductively coupled plasma emission spectrometer (ICP-OES). The active catalyst was exfoliated from the substrate via a strong and long-time sonication process and weighed. Then, nitric acid was applied to completely dissolve the sample to prepare the solutions with different concentrations, which were analyzed by ICP-OES.

2.6. Electrochemical measurements

Electrochemical measurement for the synthesized materials was carried out using a standard three-electrode system with a CHI-760D electrochemical workstation (CHI Instruments, Shanghai, China), using platinum foil as the counter electrode and saturated calomel electrode as the reference electrode (SCE). When the samples were tested for HER and OER in 1.0 M KOH, 0.5 M H_2SO_4 and 1.0 M PBS solutions using linear voltammetric scanning (LSV) technique, the scan rates were all controlled at 5 mV s^{-1}. The potentials measured can be converted into a reversible hydrogen electrode (RHE) scale by the following formula: $E_{RHE} = E_{SCE} + E^0_{SCE} + 0.059$ pH, where E_{SCE} is the experimentally measured potential and $E^0_{SCE} = 0.242$ V. In addition, iR compensation were applied for all electrochemical measurements to eliminate the effect of ohmic resistance on the as-measured reaction currents obtained from the tests [48]. All the measurements were carried out at room temperature.

3. Results and discussion

Scheme. 1 illustrates the stepwise preparation of Fe-Ni_3S_2@$FeNi_3$ and the detailed procedures are described in experimental section. Briefly, TAA, urea and NH_4F were dissolved in deionized water by ultrasonic agitation to obtain a clear and transparent solution. Then, the solution and a clean $FeNi_3$ foam were transferred into a Teflon-lined stainless steel autoclave, and maintained at different times and 120 °C to obtain Fe-Ni_3S_2@$FeNi_3$. The color of the $FeNi_3$ foam changed from silvery grey to black after hydrothermal treatment at different times as shown in Fig. S1.

The surface morphologies of Fe-Ni_3S_2@$FeNi_3$ samples prepared from different reaction times are shown in Fig. 1. When the reaction time is controlled at 8 h, the obtained Fe-Ni_3S_2-8 has a relatively regular and closely compacted rod-like array structure (Fig. 1d-f). After shortening the reaction time to 4 h, the obtained Fe-Ni_3S_2@$FeNi_3$-4 is no longer arranged in rod-like array, but displays the irregular block structures (Fig. 1a-c). After prolonging the reaction time, the obtained Fe-Ni_3S_2@$FeNi_3$-12 sample still presents a regular and compact rod-like array structure. In addition, a small amount of irregular pine-like substance adheres on the surface of the rod-like array (Fig. 1g-i). As shown in Fig. 1d, the size of rod-like Fe-Ni_3S_2@$FeNi_3$-8 is basically above 200 nm. At the same time, the rods are firmly anchored on the $FeNi_3$ foam to form a very strong 3D structure, which makes Fe-Ni_3S_2@$FeNi_3$-8 a very strong and stable catalyst. As control experiments, Ni-free $Fe(OH)_3$ and Fe-free Ni_3S_2 were prepared by replacing $FeNi_3$ foam with Fe foam and Ni foam, respectively, and controlling other experimental parameters the same as those for preparing Fe-Ni_3S_2@$FeNi_3$ (Fig. S2). It can be observed that Ni_3S_2 exhibits a small amount of irregular unsmooth structures on the Ni foam (Fig. S2d-f), and a large number of $Fe(OH)_3$ spheres with different sizes are generated on the Fe foam.

In addition, Fe-Ni_3S_2 nanorods were characterized by TEM. As can be seen from Fig. 2a, Fe-Ni_3S_2@$FeNi_3$-8 sample has a clear rod-like morphology and these rods have a relatively large diameter to allow the catalyst to maintain long-term stability during the catalytic process. Fig. 2c and Fig. 2d show high resolution TEM (HRTEM) images of a single Fe-Ni_3S_2@$FeNi_3$-8 rod. It can be seen that the lattice fringes in the figure are very clear and easy to identify, which fully demonstrates that Fe-Ni_3S_2@$FeNi_3$-8 has good crystallinity. In addition, it is important that the exposed crystal faces of the catalyst are beneficial to improve the catalytic activity, the lattice spacings are 0.184 nm, 0.238 nm, and 0.288 nm, respectively, which should correspond to the (1 1 3), (0 0 3), and (1 1 0) crystalline planes of Ni_3S_2 (PDF no.44–1418). It is worth noting that the lattice fringe spacing in Fig. 2c and Fig. 2d is slightly larger than the standard spacings of Ni_3S_2 (0.183 nm, 0.238 nm and 0.287 nm), which may be due to the small substitution of Fe for Ni. The bright ring composed of discrete spots in the selected area electron diffraction (SAED) image of Fe-Ni_3S_2@$FeNi_3$-8 in Fig. 3b can well correspond to the (1 1 3), (0 0 3), and (1 1 0) crystal planes. These characterizations fully demonstrate the successful formation of Fe-Ni_3S_2, which are consistent with the characterization of XRD (Fig. 3). In addition, the energy-dispersive spectroscopy (EDS) elemental mapping images were used to verify the distribution of Fe, Ni, S elements in Fe-Ni_3S_2@$FeNi_3$-8 rods. It can be seen from Fig. 2e-h that these three elements are evenly distributed in the rods of Fe-Ni_3S_2@$FeNi_3$-8. The uniform distribution of the elements is very advantageous for uniform distribution of the active sites on the catalyst.

The crystal structure of Fe-Ni_3S_2@$FeNi_3$-8 was further studied by X-ray diffraction (XRD). As can be seen from Fig. 3a, the diffraction peaks of Fe-Ni_3S_2@$FeNi_3$-8 at 21.83°, 31.14°, 37.79°, 49.77°, 55.23°, 73.09° and 77.93° should correspond to (1 0 1), (1 1 0), (0 0 3), (1 1 3), (1 2 2), (2 1 4) and (4 0 1) crystalline planes of Ni_3S_2 (PDF no. 44–1418), respectively. The diffraction peaks at 44.40°, 51.86° and 76.42° can be assigned to the (1 1 1), (2 0 0) and (2 2 0) crystalline planes of $FeNi_3$. In addition, no diffraction peaks of other impurity phases were detected, particularly diffraction peaks of Fe-based sulfides. This also indicates that the Fe element is likely to be doped in the lattice of Ni_3S_2 in a stable state, and the weight percentage of Fe in Fe-Ni_3S_2@$FeNi_3$-8 was detected to be 1.06% by ICP-OES. In addition, the Fe contents of Fe-Ni_3S_2@$FeNi_3$-(4, 12) were found to be 1.02% and 1.03% by the same analytical method. Therefore, it can be concluded that a trace amount of Fe-doped Ni_3S_2 electrode has been successfully prepared by a simple one-step hydrothermal method.

XPS was also utilized to characterize the chemical state and

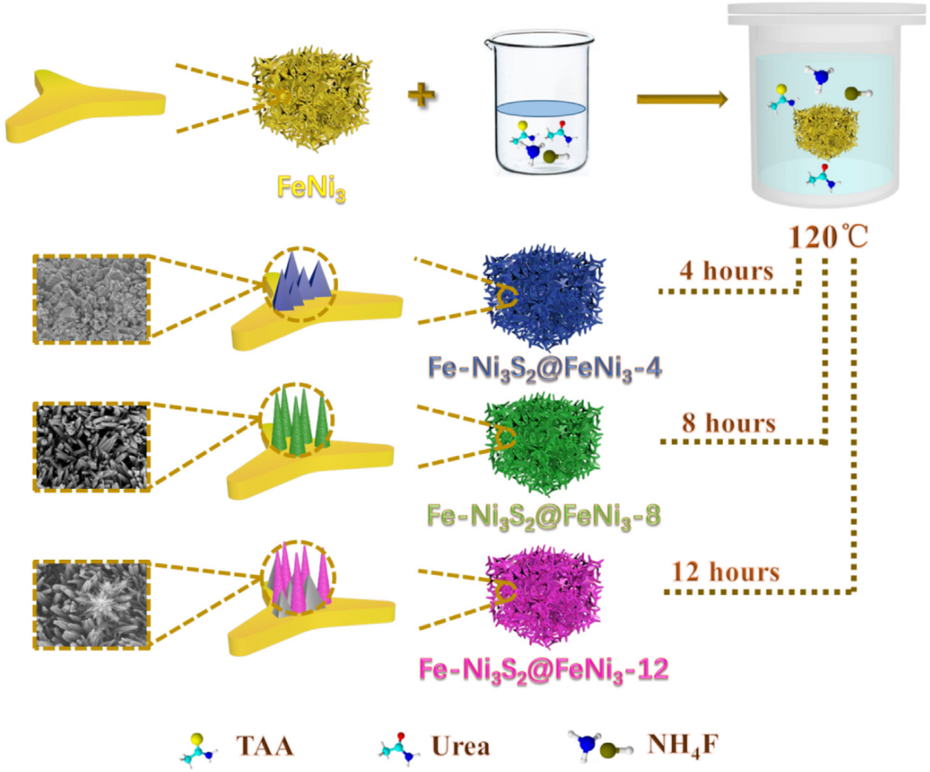

Scheme 1. Schematic illustration for the stepwise preparation of Fe-Ni_3S_2@$FeNi_3$-(4, 8, 12) at different reaction times.

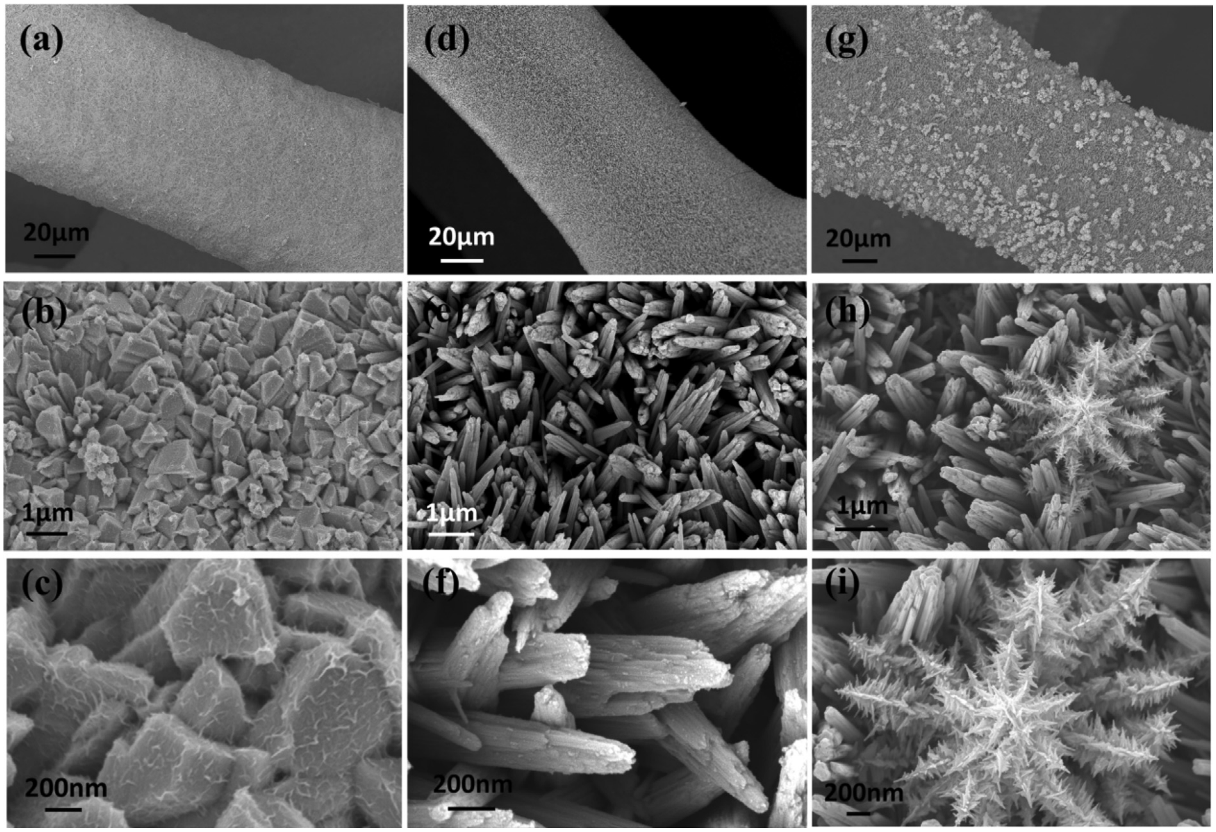

Fig. 1. (a-c) SEM images of Fe-Ni_3S_2@$FeNi_3$-4. (d-f) SEM images of Fe-Ni_3S_2@$FeNi_3$-8. (g-i) SEM images of Fe-Ni_3S_2@$FeNi_3$-12.

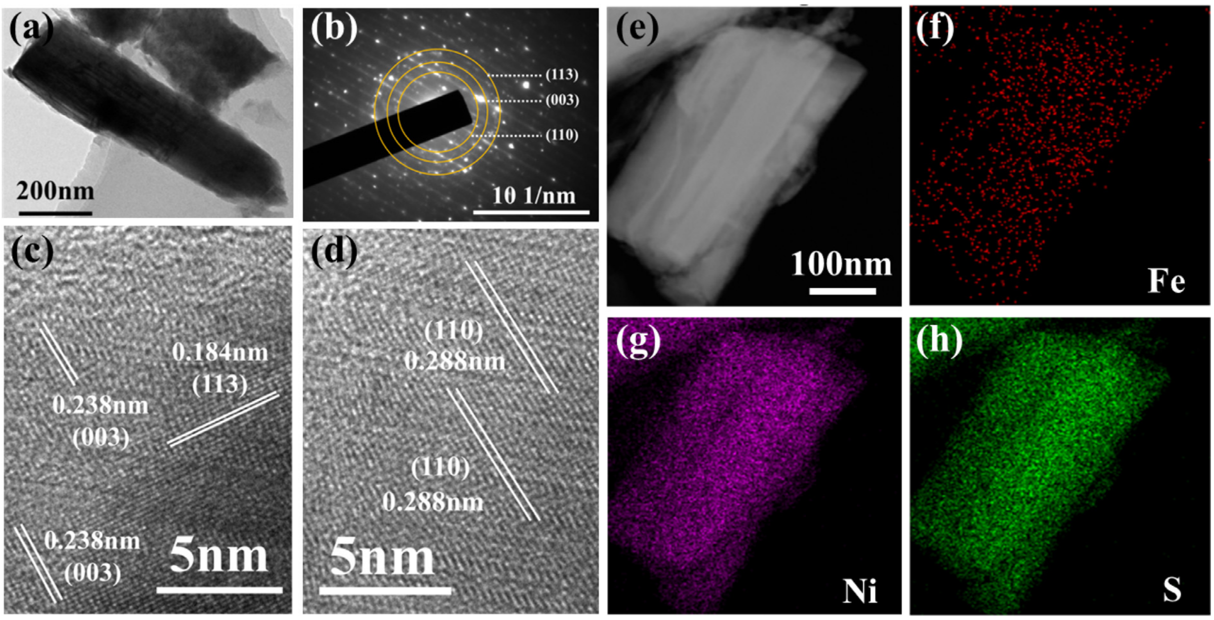

Fig. 2. (a) TEM image of Fe-Ni_3S_2@$FeNi_3$-8 rods. (b) SAED pattern of Fe-Ni_3S_2@$FeNi_3$-8 rods. (c-d) HRTEM images of Fe-Ni_3S_2@$FeNi_3$-8 rods. (e-h) STEM image and the corresponding elemental mapping images of Fe, Ni, and S in Fe-Ni_3S_2@$FeNi_3$-8.

elemental composition of the prepared samples. The two characteristic peaks at 855.6 eV and 873.4 eV as observed in Fig. 3d should correspond to $Ni_{3/2}$ and $Ni_{1/2}$, respectively, while two satellite peaks at 861.3 eV and 879.2 eV belong to the rocking peak of Ni. These observations all prove that Ni in Fe-Ni_3S_2 is in the state of Ni^{2+}. Moreover, a peak at 852.6 eV can be assigned to Ni_3S_2 or Ni[49,50]. The existence of Fe element was strongly confirmed by XPS characterization. It can be seen from Fig. 3e that there are two distinct peaks in the Fe 2p curve after fitting, which are located at 706.1 eV and 712.3 eV respectively, indicating the presence of Fe^{2+} and Fe^{3+}[51,52]. This phenomenon also strongly demonstrates that the Fe element has been successfully doped into Ni_3S_2. As shown in Fig. 3f, the two peaks at 161.7 eV and 162.7 eV can be assigned to the S $2p_{3/2}$ and S $2p_{1/2}$, evidencing the presence of S^{2-} in Fe-Ni_3S_2, respectively. The peak at 168.5 eV can be attributed to the sulfate species produced by the oxidation of Fe-Ni_3S_2 in the air[53,54].

In order to explore the effects of reaction time on the performance of the catalyst, the catalytical performance Fe-Ni_3S_2@$FeNi_3$-4, Fe-Ni_3S_2@

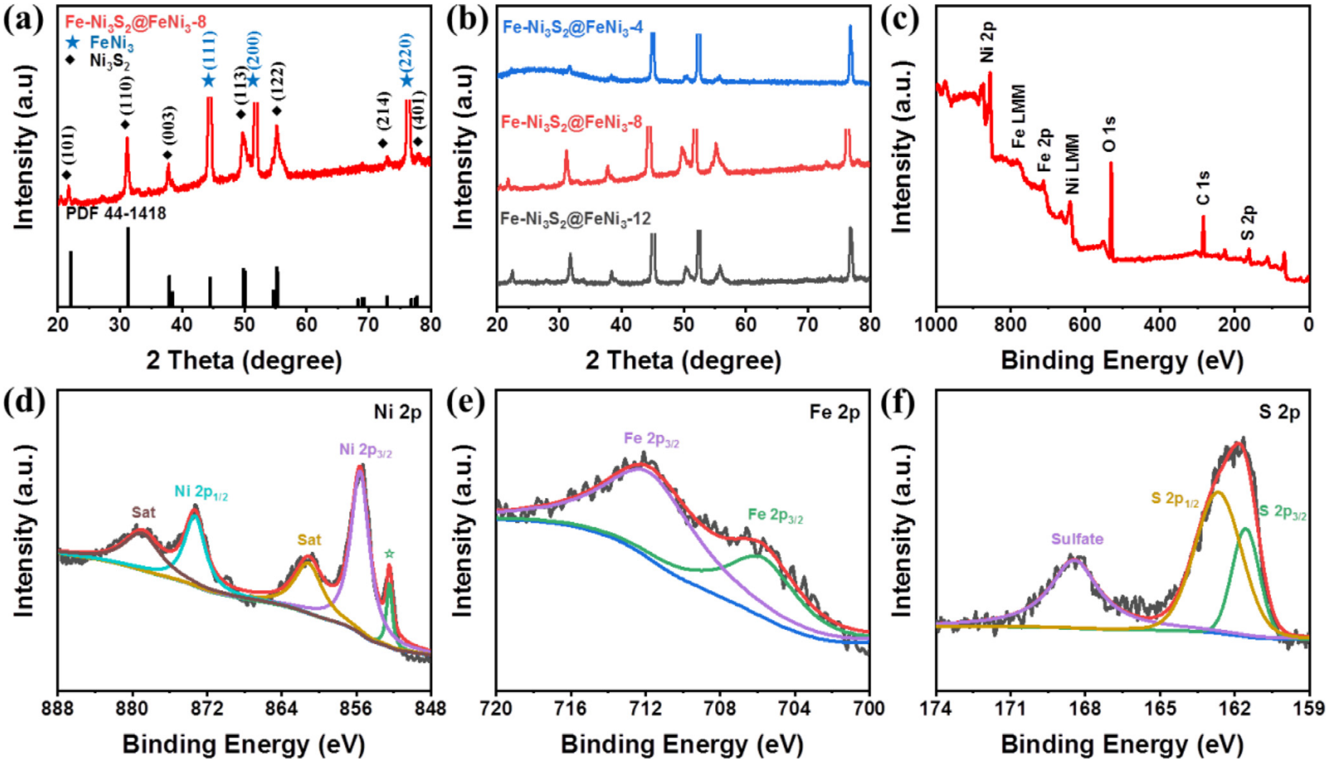

Fig. 3. (a) XRD patterns of Fe-Ni_3S_2@$FeNi_3$-8. (b) XRD patterns of Fe-Ni_3S_2@$FeNi_3$-4, Fe-Ni_3S_2@$FeNi_3$-8 and Fe-Ni_3S_2@$FeNi_3$-12. (c) XPS survey spectrum of Fe-Ni_3S_2@$FeNi_3$-8. High-resolution XPS spectra of (d) Ni 2p, (e) Fe 2p, and (f) S 2p regions for Fe-Ni_3S_2@$FeNi_3$-8.

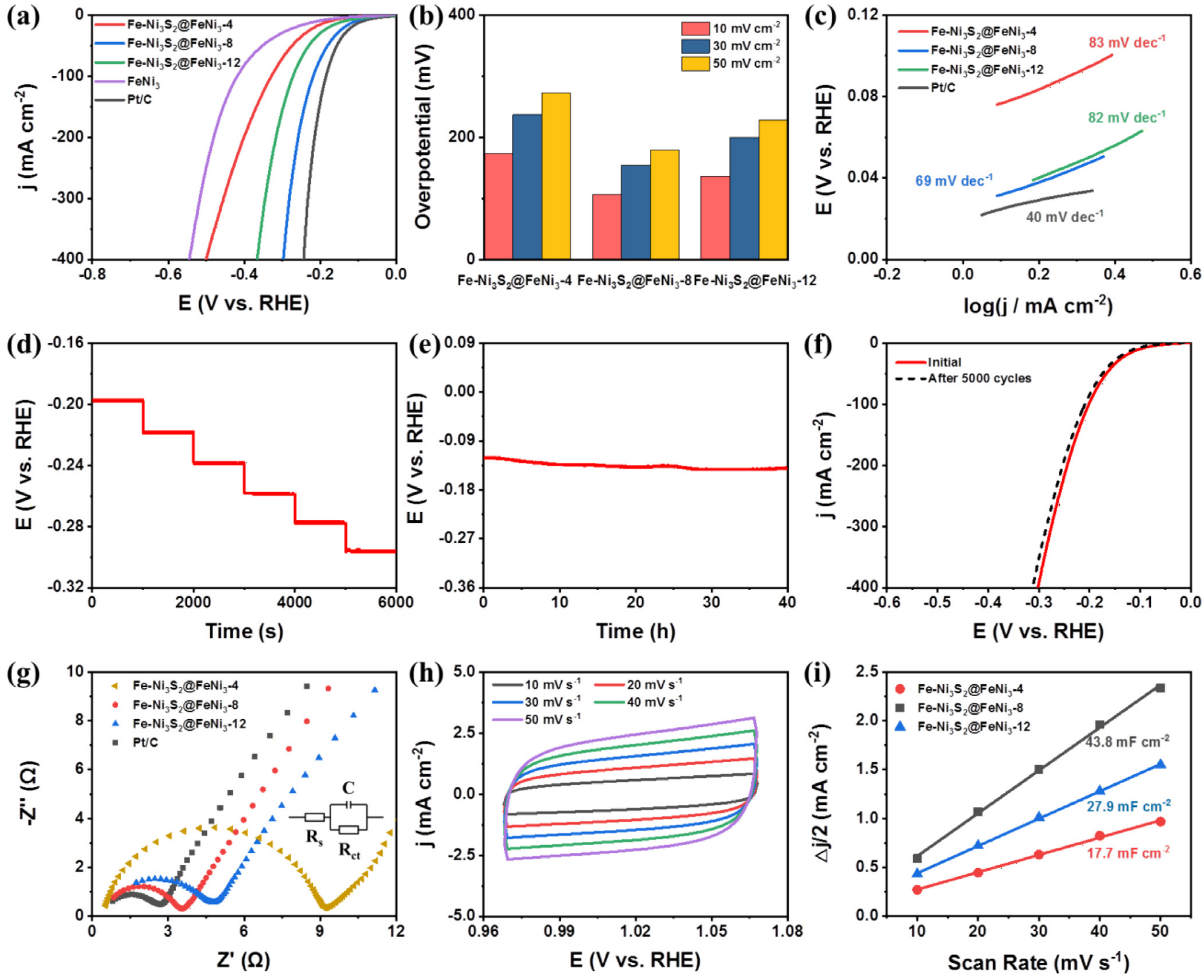

Fig. 4. Electrochemical HER properties of the electrocatalysts in 1.0 M KOH solution. (a) Polarization curves (iR-corrected) at a scan rate of 5 mV s^{-1}, (b) potentials corresponding to different current densities (10, 30, 50 mA cm^{-2}) and (c) Tafel plots of Fe-Ni_3S_2@$FeNi_3$-4, Fe-Ni_3S_2@$FeNi_3$-8, Fe-Ni_3S_2@$FeNi_3$-12 and Pt/C. (d) Multi-current process of Fe-Ni_3S_2@$FeNi_3$-8. The current density started at 50 mA cm^{-2} and finished at 100 mA cm^{-2}, with an increment of 10 mA cm^{-2} every 1000 s without iR correction. (e) The chronopotentiometry curve of Fe-Ni_3S_2@$FeNi_3$-8 under a constant current density of 10 mA cm^{-2} without iR correction. (f) Polarization curves of Fe-Ni_3S_2@$FeNi_3$-8 before and after 5000 CV cycles without iR correction. (g) Electrochemical impedance spectra (EIS) of Fe-Ni_3S_2@$FeNi_3$-4, Fe-Ni_3S_2@$FeNi_3$-8 and Fe-Ni_3S_2@$FeNi_3$-12 electrodes recorded at an applied potential of 0.5 V (V vs. RHE) with a frequency range of 100 kHz to 10 mHz; the inset of Fig. 4g is the corresponding equivalent circuit diagram. (h) Cyclic voltammograms (CVs) for Fe-Ni_3S_2-8 at scan rates of 10, 20, 30, 40 and 50 mV s^{-1}. (i) Current densities determined at a potential of 0.218 V (V vs. RHE) as a function of scan rate for Fe-Ni_3S_2@$FeNi_3$-4, Fe-Ni_3S_2@$FeNi_3$-8 and Fe-Ni_3S_2@$FeNi_3$-12.

$FeNi_3$-8 and Fe-Ni_3S_2@$FeNi_3$-12 obtained from different reaction time of 4, 8 and 12 h were measured. By observing the polarization curves of the iR compensation obtained using a standard three-electrode system, it is found that Fe-Ni_3S_2-8 has the best catalytic performance (Fig. 4a). To obtain the current density of 10 mA cm^{-2}, Fe-Ni_3S_2@$FeNi_3$-(4, 12) require the overpotential of 174 mV and 136 mV, respectively, which is much higher than the 105 mV required for Fe-Ni_3S_2@$FeNi_3$-8 (Fig. 4b), it is obviously that Fe-Ni_3S_2@$FeNi_3$-8 exhibits the highest catalytic activity.

In addition to the intuitive observation of catalyst performance from the LSV curve, the Tafel slope value is also an important indicator for evaluating the performance of a catalyst, which can be calculated from the corresponding LSV curve by the Tafel slope equation ($\eta = b \log j + a$, where η represents overpotential, b represents Tafel slope, and j represents current density). When the electrolyte solution is 1.0 M KOH solution, the Tafel slopes of Fe-Ni_3S_2@$FeNi_3$-4, Fe-Ni_3S_2@$FeNi_3$-8 and Fe-Ni_3S_2@$FeNi_3$-12 are 83 mV dec^{-1}, 69 mV dec^{-1} and 82 mV dec^{-1}, respectively. It can be found that the value of Fe-Ni_3S_2@$FeNi_3$-8 is significantly lower than the other two samples (Fig. 4c), and Fig. S4b shows that Fe-Ni_3S_2@$FeNi_3$-8 has a smaller Tafel slope value compared to Ni_3S_2 and $Fe(OH)_3$, indicating a faster HER kinetics of Fe-Ni_3S_2@$FeNi_3$-8.

In addition to the above characterizations, in order to more fully explore the performance of Fe-Ni_3S_2@$FeNi_3$-8 for HER, the stability tests were also performed. Firstly, the multi-step chronoamperometry measurement was carried out. As shown in Fig. 4d, the multi-step chronoamperometry curve reflects that Fe-Ni_3S_2@$FeNi_3$-8 can respond rapidly to different current densities and reach a stable level quickly, so it can be seen that Fe-Ni_3S_2@$FeNi_3$-8 has good catalytic activity. The geometric current density gradually increases from 50 mA cm^{-2} to 100 mA cm^{-2} with a increasing step of 10 mA cm^{-2} for every 1000 s. At the same time, it can be observed from Fig. S15 that when the current density changes, the response speed of HER does not exceed 0.01 s, indicating that Fe-Ni_3S_2@$FeNi_3$-8 has a very fast electron transfer rate[55]. Secondly, the long-term stability test of Fe-Ni_3S_2@$FeNi_3$-8 was carried out using the chronopotentiometry. It was found

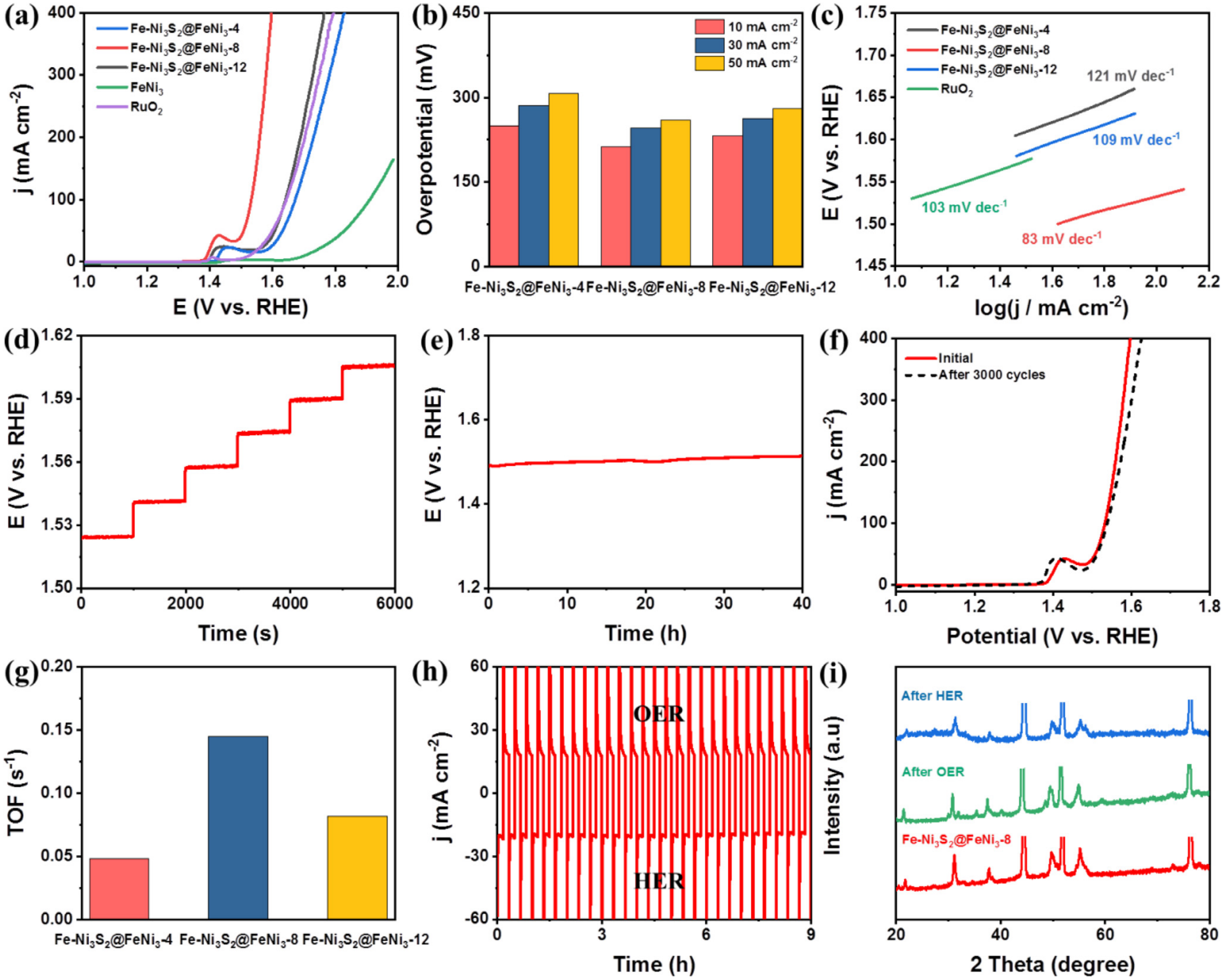

Fig. 5. Electrochemical OER properties of the electrocatalysts in 1.0 M KOH solution. (a) Polarization curves (iR-corrected) at a scan rate of 5 mV s^{-1}. (b) Potentials at different current densities (10, 30 and 50 mA cm^{-2}). (c) Tafel plots of Fe-Ni$_3$S$_2$@FeNi$_3$-4, Fe-Ni$_3$S$_2$@FeNi$_3$-8, Fe-Ni$_3$S$_2$@FeNi$_3$-12 and RuO$_2$. (d) Multi-current process of Fe-Ni$_3$S$_2$@FeNi$_3$-8. The current density started from 50 mA cm^{-2} and finished at 100 mA cm^{-2}, with an increment of 10 mA cm^{-2} every 1000 s without iR correction. (e) The chronopotentiometry curve of Fe-Ni$_3$S$_2$@FeNi$_3$-8 under a constant current density of 10 mA cm^{-2} without iR correction. (f) Polarization curves of Fe-Ni$_3$S$_2$@FeNi$_3$-8 before and after 3000 cycles without iR correction. (g) The values of TOF of Fe-Ni$_3$S$_2$@FeNi$_3$-4, Fe-Ni$_3$S$_2$@FeNi$_3$-8 and Fe-Ni$_3$S$_2$@FeNi$_3$-12. (h) Chronoamperomeric curve obtained with Fe-Ni$_3$S$_2$@FeNi$_3$-8 electrode in 1.0 M KOH, and the potential operated on the working electrode is changed intermittently between −0.14 and 1.51 V versus RHE every 10 min. (i) XRD spectra of Fe-Ni$_3$S$_2$@FeNi$_3$-8 after 40 h long term electrolysis for HER and OER.

that Fe-Ni$_3$S$_2$@FeNi$_3$-8 could maintain stable catalytic activity at the current density of 10 mA cm^{-2} for 40 h, and the overpotential decreased slightly (Fig. 4e).

SEM characterization of samples subjected to long-term stability test revealed that the sample remained substantially in morphology with almost no collapse (Fig. S10a), directly indicating that the rod-like array structure has very good firmness, thereby fully demonstrating the excellent stability of Fe-Ni$_3$S$_2$@FeNi$_3$-8. In addition, after performing a 40 h long-term stability test on Fe-Ni$_3$S$_2$@FeNi$_3$-8, Fe, Ni, and S elements can still be found (Fig. S10). Finally, 5,000 cyclic voltammetry (CV) cycles of Fe-Ni$_3$S$_2$@FeNi$_3$-8 were performed at a scan rate of 5 mV s^{-1} with the voltage range from 0 to −0.2 V (relative to RHE) in a 1.0 M KOH solution. It can be seen from Fig. 5f that the performance of Fe-Ni$_3$S$_2$@FeNi$_3$-8 is almost unchanged, and the original catalytic activity is maintained. In addition, the XRD peaks were basically consistent before and after HER test, showing that Fe-Ni$_3$S$_2$@FeNi$_3$-8 has a good stability and long-term durability (Fig. 5i).

In addition, the kinetics at the interface of electrolyte and electrocatalyst of Fe-Ni$_3$S$_2$@FeNi$_3$-8 were analyzed by electrochemical impedance spectroscopy (EIS) to further explore the effect of different reaction times on the activity of catalysts. According to the fitting equivalent circuit model, the charge transfer resistances of Fe-Ni$_3$S$_2$@FeNi$_3$-(4, 8, 12) were derived to be 8.39, 3.23 and 4.61 Ω, respectively (Fig. 4g). By comparison, it can be found that when the experimental time is extended from 4 h to 8 h, the R$_{ct}$ value is reduced from 8.39 Ω to 3.23 Ω. Whereas, when the experimental time is further extended from 8 h to 12 h, the R$_{ct}$ value increased from 3.23 Ω to 4.61 Ω. These results indicate that Fe-Ni$_3$S$_2$@FeNi$_3$-8 has the smallest value of R$_{ct}$, which indicates that it has the highest charge transfer rate. Fe-Ni$_3$S$_2$@FeNi$_3$-(4, 12) also have small R$_{ct}$ values, which demonstrates a high-quality bonding between FeNi$_3$ foam and rod-shaped Fe-Ni$_3$S$_2$. In addition, the Rct value of Fe-Ni$_3$S$_2$@FeNi$_3$-8 is the smallest compared to the Rct values of most other catalysts reported recently (Table S8).

The HER catalytic activity of Fe-Ni$_3$S$_2$@FeNi$_3$-(4, 8, 12) was further evaluated by double-layer capacitance (C$_{dl}$). The CV curves of the samples were recorded at different scan rates (10, 20, 30, 40 and 50 mV s^{-1} as shown in Fig. 4h and Fig. S6. Based on the CV curve of each sample collected, the corresponding C$_{dl}$ of Fe-Ni$_3$S$_2$@FeNi$_3$-(4, 8,

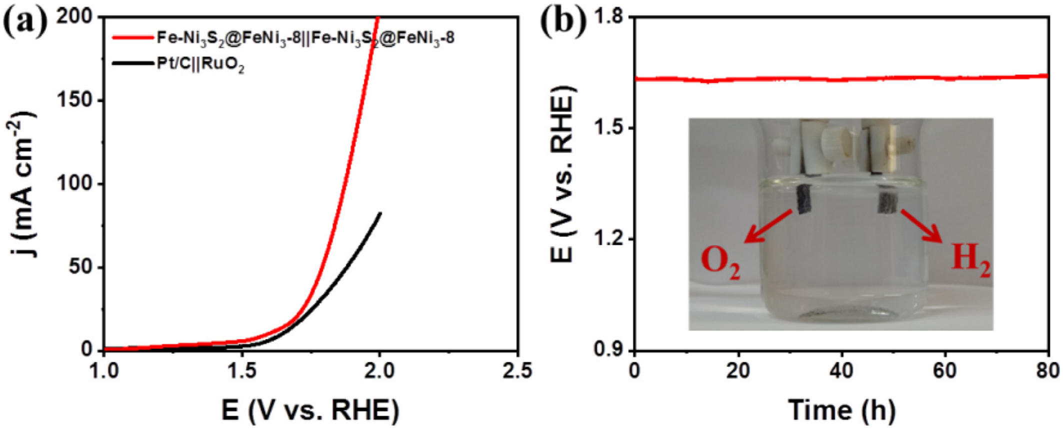

Fig. 6. (a) Polarization curves (without iR compensation) for water electrolysis of Fe-Ni_3S_2@$FeNi_3$-8‖Fe-Ni_3S_2@$FeNi_3$-8 and Pt‖RuO_2 in a two-electrode configuration at a scan rate of 5 mVs^{-1}. (b) Chronopotentiometric response curve of Fe-Ni_3S_2@$FeNi_3$-8‖ Fe-Ni_3S_2@$FeNi_3$-8 at a current density of 10 mA cm^{-2} for 80 h. All experiments were carried out in 1.0 M KOH solution. Inset: optical photograph of the Fe-Ni_3S_2@$FeNi_3$-8‖ Fe-Ni_3S_2@$FeNi_3$-8.

12) were calculated by linear fitting to be 17.7, 43.8, and 27.9 mF cm^{-2}, respectively (Fig. 4i). Then, the electrochemical surface area (ECSA) of the sample is calculated according to the equation ECSA = C_{dl} / C_s, where ECSA is proportional to C_{dl}, and Cs is a constant whose value is reported to be 0.040 mF cm^{-2}. The ECSA values of Fe-Ni_3S_2@$FeNi_3$-(4, 8, 12) are calculated to be 442.5, 1095.0 and 697.5 cm^2, respectively, among which the ECSA value of Fe-Ni_3S_2@$FeNi_3$-8 is the highest. This phenomenon fully demonstrates that Fe-Ni_3S_2@$FeNi_3$-8 could expose more catalytical active sites, thus exhibit more excellent catalytic activity for HER. In addition, it can be seen that the C_{dl} value of Fe-Ni_3S_2@$FeNi_3$-8 is larger than those recently reported as shown in Table S7, indicating the higher electrochemical catalytic surface area.

In order to comprehensively understand the performance of Fe-Ni_3S_2@$FeNi_3$-(4, 8, 12), we also explored their performance for OER at a scan rate of 5 mV s^{-1} in 1.0 M KOH solution and the corresponding LSV curves are shown in Fig. 6a. The overpotentials of Fe-Ni_3S_2@$FeNi_3$-(4, 8, 12) are found to be 250, 213 (The overpotential 213 mV was obtained from Fig. S19 [21]) and 232 mV respectively to achieve the current density of 10 mA cm^{-2}. It is obviously that the Fe-Ni_3S_2@$FeNi_3$-8 requires the smallest overpotential among these three samples (Fig. 5b). The oxidation peak at about 1.42 V should be attributed to the oxidation of nickel in Fe-Ni_3S_2@$FeNi_3$ during the OER process [56,57]. The peaks position varied with different reaction time of Fe-Ni_3S_2@$FeNi_3$ can be attributed to the various electronic transmission capacity of different Fe-Ni_3S_2@$FeNi_3$ samples [56,58–60]. Therefore, it can be concluded that Fe-Ni_3S_2@$FeNi_3$-8 has the best catalytic activity for OER in an alkaline environment. According to the LSV curve of Fe-Ni_3S_2@$FeNi_3$-(4, 8, 12), the corresponding Tafel slopes are 121, 83 and 109 mV dec^{-1}, among which Fe-Ni_3S_2@$FeNi_3$-8 has the smallest Tafel slope value. Such difference in the performances of Fe-Ni_3S_2@$FeNi_3$-(4, 8, 12) can be attributed to the number of active sites and the electron transport capacity of these catalysts with various amount of Fe doping obtained from different reaction time.

The stability test was also performed for more comprehensive evaluation of the performance of Fe-Ni_3S_2@$FeNi_3$-8 for OER, in the same manner as the performance test for HER. The multi-step chronoamperometry was used to test the stability of Fe-Ni_3S_2@$FeNi_3$-8 at a starting current density of 50 mA cm^{-2}. It can be seen from Fig. 5d that after reaching each of the set current density, the required overpotential can be stably maintained for 1000 s. Similar to HER, it can be seen from Fig. S15 that when the current density changes, the response time is less than 0.01 s, indicating Fe-Ni_3S_2@$FeNi_3$-8 has the fast kinetics. When the current density reaches 100 mA cm^{-2}, the catalyst still maintains good stability. Similarly, Fe-Ni_3S_2@$FeNi_3$-8 is able to maintain 93% of its initial catalytic activity after maintaining the current density of 10 mA cm^{-2} for 40 h in 1.0 M KOH (Fig. 5e), which indicates Fe-Ni_3S_2@$FeNi_3$-8 has the excellent catalytic stability for OER. SEM characterization of samples subjected to long-term stability test revealed that the sample remained substantially in morphology with almost no collapse and the distribution of Fe, Ni, S is also very uniform (Fig. S11). In addition, Fe-Ni_3S_2@$FeNi_3$-8 can maintain ultra-high catalytic performance after 3,000 CV cycles (Fig. 5f). Furthermore, the position of this oxidation peak moves slightly to a lower potential after a 3000 cycles tests, which can be attributed to the mild activation during the long-time usage, leading to the faster electron transfer with the catalyst. Based on these test results, it can be clearly seen that Fe-Ni_3S_2@$FeNi_3$-8 has an extremely high catalytic performance and excellent stability. There are two main reasons why Fe-Ni_3S_2@$FeNi_3$-8 is stable after long-term oxidation in OER: Firstly, the combination of rod-shaped Fe-Ni_3S_2 and $FeNi_3$ foam is strong enough; Secondly, Fe-Ni_3S_2@$FeNi_3$-8 has a stable crystal structure, its phase was not destroyed as evidenced by the XRD patterns of the samples before and after the long-term stability test (Fig. 5i).

In addition, it can be noted from Fig. S7 that there are two reversible redox peaks of Ni^{3+}/Ni^{2+} in the potential range from 1.1 V to 1.6 V, from which the turnover frequency (TOF) values of Fe-Ni_3S_2@$FeNi_3$-(4, 8, 12) are calculated to be 0.048, 0.145 and 0.082 s^{-1}, among which Fe-Ni_3S_2@$FeNi_3$-8 has the highest TOF value (Fig. 5g). The higher value of TOF reflects that the catalyst has the better intrinsic activity, indicating that the catalyst has more active sites and better catalytic performance. This phenomenon also confirms that Fe-Ni_3S_2@$FeNi_3$-8 has the best kinetics of OER.[61,62] XPS characterization of samples subjected to long-term stability tests for OER showed that a new peak appears at 724.7 eV, which can be attributed to Fe $2p_{1/2}$, showing that part of Fe^{2+} ions have been converted into Fe^{3+} ions (Fig. S12). In addition to this, XRD characterization for Fe-Ni_3S_2@$FeNi_3$-8 after OER revealed that iron-based hydroxide was newly formed (Fig. 5i). Therefore, it can be concluded that it should be Fe element that contributes to the improvement of catalyst performance in the form of iron-based hydroxide in the process of OER.

In 2015, Martindale and Reisner proposed an innovative concept for electrochemical regeneration of the active sites on iron oxide/hydroxide composites to improve the long-term stability of the electrode, thus demonstrating the relationship between OER and HER has a stable reversibility [63]. Based on this concept the reversibility of the Fe-Ni_3S_2@$FeNi_3$-8 electrode was also studied. Wherein, the bias of the polarization applied on the Fe-Ni_3S_2@$FeNi_3$-8 working electrode was inverted every 10 min between –0.14 and 1.51 V versus RHE for HER and OER, respectively, to obtain the corresponding current density (j), through which the stability of electrode can be directly assessed. It can be observed from Fig. 5h that when a potential of -0.14 V is applied to the

Fe-Ni_3S_2@$FeNi_3$-8 electrode for HER, the current density of 20 mA cm^{-2} is rapidly generated and then quickly stabilized. When a potential of 1.51 V was applied to the Fe-Ni_3S_2@$FeNi_3$-8 electrode for OER, a large positive current density was also quickly generated, and stabilized at 20 mA cm^{-2}. It can be seen that during the reversibility test, Fe-Ni_3S_2@$FeNi_3$-8 can produce a relatively stable current density of 20 mA cm^{-2} for 54 cycles of HER and OER. This phenomenon fully illustrates Fe-Ni_3S_2@$FeNi_3$-8 has excellent reversibility.

In order to more objectively assess the catalytic activity of the catalyst, a number of control experiments were also carried out for Pt/C, RuO_2, $FeNi_3$, Ni_3S_2 and $Fe(OH)_3$. Among them, Pt/C and RuO_2 are powders, which need to be deposited on $FeNi_3$ foam as working electrodes, and their loadings at the electrodes are found to be 0.83 and 0.82 mg cm^{-2}, respectively. As shown in Fig. 4a, the commercial Pt/C exhibits superior catalytic activity for HER, requiring only an ultra-low overpotential of 87 mV to provide the current density of 10 mA cm^{-2}, and the value of Tafel slope is only 40 mV dec^{-1} (Fig. 4c). It can be seen that Fe-Ni_3S_2@$FeNi_3$-8 exhibits comparable catalytic activity to that of Pt/C. As shown in Fig. 5a, the commercial RuO_2 for OER requires an overpotential of 293 mV to provide a current density of 10 mA cm^{-2} and the value of Tafel slope is 103 mV dec^{-1} (Fig. 5c). Obviously, Fe-Ni_3S_2@$FeNi_3$-8 has superior performance to commercial RuO_2. In addition, the catalytic activities of Fe-Ni_3S_2@$FeNi_3$-8 for HER and OER are comparable or superior to other metal catalysts recently reported as summarized in Table S1 and Table S2. For HER, for example, Liu et al. prepared (Ni, Fe)S_2/MoS_2 through an interfacial engineering strategy that required an overpotential of 130 mV to provide the current density of 10 mA cm^{-2} [64]. In addition, Yu et al. also constructed a nanosheet structure of Sn-Ni_3S_2/NF by doping Sn element into Ni_3S_2. To achieve the current density of 10 mA cm^{-2}, an overpotential of 137 mV is required [65]. For OER, Xiong et al. prepared a $(Fe_{0.5}Ni_{0.5})S_2$ nanocrystal/carbon black composite that required an overpotential of 270 mV at the current density of 10 mA cm^{-2} [38]. Joang et al. synthesized 2D ultra-thin ternary $FeNiS_2$ nanosheets (NSs) that required an overpotential of 310 mV to achieve the current density of 10 mA cm^{-2} [66]. The catalytic activities of these catalysts are significantly lower than that of Fe-Ni_3S_2@$FeNi_3$-8 in this paper. $FeNi_3$ requires an overpotential of 472 mV to provide a current density of 10 mA cm^{-2} for OER, while Fe-Ni_3S_2@$FeNi_3$-8 requires only 213 mV (Fig. 5a). In addition, Ni_3S_2 was prepared without Fe element as a control group by the same experimental parameters for Fe-Ni_3S_2@$FeNi_3$-8, but replaced $FeNi_3$ foam with Ni foam. It can be found that for HER and OER, Ni_3S_2 requires overpotential of 161 mV and 282 mV to provide the current density of 10 mA cm^{-2}, respectively (Fig. S4a and Fig. S4d), these are much higher than that of Fe-Ni_3S_2@$FeNi_3$-8. Fe doping in Ni_3S_2 can adjust the electronic structure of Ni_3S_2, improve the conductivity of the catalyst and form more active sites [67], therefore Fe-Ni_3S_2@$FeNi_3$-8 has better catalytic performance. Fe foam was used as a substrate, and a control sample was prepared by the same method. By analyzing the composition of the sample prepared from Fe foam, it was found that $Fe(OH)_3$ was synthesized. Through testing using a three-electrode system, $Fe(OH)_3$ requires overpotentials of 203 mV and 292 mV to achieve the current density of 10 mA cm^{-2} for HER and OER, respectively (Fig. S4a and Fig. S4b), which are much larger than 105 mV and 213 mV required by Fe-Ni_3S_2@$FeNi_3$-8. Table S3 and Table S4 compare othe catalytic performances of our catalyst and other materials reported in the literature for HER and OER.

Since Fe-Ni_3S_2@$FeNi_3$-8 has excellent catalytic properties for HER and OER, it can be considered as a cathode and an anode assembled into one two-electrode system for overall water splitting in 1.0 M KOH solution. In addition, the performance of a two-electrode system composed of Pt/C as a cathode and RuO_2 as an anode for HER and OER was also tested under the same conditions. It can be seen from Fig. 6a that the Fe-Ni_3S_2@$FeNi_3$-8‖ Fe-Ni_3S_2@$FeNi_3$-8 system only needs a potential of 1.59 V to provide the current density of 10 mA cm^{-2}. In contrast, the Pt/C‖RuO_2 system requires a voltage of 1.64 V to deliver the current density of 10 mA cm^{-2}. The total hydrolyzing activity of Fe-Ni_3S_2@$FeNi_3$-8 is not only better than the precious metal Pt/C‖RuO_2 system, but also superior to most of the materials recently reported. For example, Feng prepared EG/Ni_3Se_2/Co_9S_8 that required a voltage of 1.62 V to provide the current density of 10 mA cm^{-2}[68]. $NiCo_2S_4$ nanowire array synthesized by Shanmugam required a higher voltage of 1.68 V to provide the current density of 10 mA cm^{-2}[69]. In addition, it can be clearly seen in Fig. 6b that the bubbles of H_2 and O_2 are continuously emerging on the cathode and anode. In addition, the durability of the overall water splitting of Fe-Ni_3S_2@$FeNi_3$-8 was tested. It can be seen from Fig. 6b that after durability test for 80 h, 93% of the initial catalytic activity was still maintained.

The performances of samples for HER were tested in 0.5 M H_2SO_4 solution. Fe-Ni_3S_2@$FeNi_3$-8 only requires overpotential of 48 mV to provide the current density of 10 mA cm^{-2} (Fig. S8a). This is due to the fact that HER kinetics are more favorable at lower pH conditions[70]. The activities of samples follow the trend of Pt/C (η_{10} = 45 mV) > Fe-Ni_3S_2@$FeNi_3$-8 (η_{10} = 48 mV) > Fe-Ni_3S_2@$FeNi_3$-12 (η_{10} = 58 mV) > Fe-Ni_3S_2@$FeNi_3$-4 (η_{10} = 70 mV) > Ni_3S_2 (η_{10} = 114 mV) (Table S5). The catalytic activity of Fe-Ni_3S_2@$FeNi_3$-8 under acidic conditions is better than most of the previously reported materials (Table S1). In addition, the values of Tafel slope and Rct of Fe-Ni_3S_2@$FeNi_3$-8 are also lower than those of Fe-Ni_3S_2@$FeNi_3$-(4, 12) (Fig. S8). After 40 h of long-term stability test, Fe-Ni_3S_2@$FeNi_3$-8 still maintains 95% of the initial catalytic activity. Fe-Ni_3S_2@$FeNi_3$-8 still maintains the regular rods array structure after 40 h of testing as evidenced by the SEM analysis (Fig. S13a) and Fe, Ni, S elements can still be detected by element mapping technology (Fig. S13b-e). In addition, the XRD peaks of Fe-Ni_3S_2@$FeNi_3$-8 did not change substantially (Fig. S8i), which evidenced that Fe-Ni_3S_2@$FeNi_3$-8 had excellent catalytic stability in 0.5 M H_2SO_4 solution.

In addition, we further studied the catalytic properties of samplesfor HER in 1.0 M PBS neutral solution. Similarly, it can be seen from Table S6 that the order of the catalytic activity of samples for HER follows Pt/C (η_{10} = 64 mV) > Fe-Ni_3S_2@$FeNi_3$-8 (η_{10} = 83 mV) > Fe-Ni_3S_2@$FeNi_3$-12 (η_{10} = 132 mV) > Ni_3S_2 (η_{10} = 139 mV) > Fe-Ni_3S_2@$FeNi_3$-4 (η_{10} = 159 mV) > $Fe(OH)_3$ (η_{10} = 225 mV). The catalytic performance of Fe-Ni_3S_2@$FeNi_3$-8 in neutral solutions is also superior to some of the materials that have been reported recently as listed in Table S1. In addition, Fe-Ni_3S_2@$FeNi_3$-8 has lower values of Tafel slope and Rct (Fig. S9). After a long period of stability test for 40 h, Fe-Ni_3S_2@$FeNi_3$-8 still maintained 90% of the initial activity. The rod-like array structure of Fe-Ni_3S_2-8 remains almost intact after long-term stability testing (Fig. S9f) and the XRD peaks of Fe-Ni_3S_2@$FeNi_3$-8 did not change substantially (Fig. S8i). In addition, Fe, Ni, S elements can still be detected (Fig. S14). These phenomena proved that the sample had excellent long-term stability in 1.0 M PBS solution.

Due to its slow reaction kinetics and high thermodynamic voltage, OER encounters a major obstacle to affect the efficient hydrogen production in two-electrode system, therefore UOR with lower thermodynamic voltage can be a good alternative. In the presence of 0.33 M urea solution, Fe-Ni_3S_2@$FeNi_3$-8 exhibited excellent HER performance which was similar to that without urea (Fig. 7a). The catalytic activity of Fe-Ni_3S_2@$FeNi_3$-8 for UOR was studied using LSV. It can be observed that the catalytic activity of catalysts for UOR are still ranked from high to low in the order of Fe-Ni_3S_2@$FeNi_3$-8 (η_{10} = 1.40 V), Fe-Ni_3S_2@$FeNi_3$-12 (η_{10} = 1.44 V), and Fe-Ni_3S_2@$FeNi_3$-4 (η_{10} = 1.45 V), and the starting voltage of UOR is less than that of OER. In addition, after modification by Fe-Ni_3S_2, the catalytic activity of Fe-Ni_3S_2@$FeNi_3$-8 is much higher than that of $FeNi_3$ (Fig. 7b).

The catalytic activity of Fe-Ni_3S_2@$FeNi_3$-8 for UOR and HER were further tested by multi-step chronoamperometry from 20 to 90 mA cm^{-2}, with an increasing step of 10 mA cm^{-2} for every 1000 s. For every current density changes, Fe-Ni_3S_2@$FeNi_3$-8 can quickly respond and stabilize (Fig. 7d and Fig. S16b). Fe-Ni_3S_2-8 has a fast response speed of less than 0.01 s for HER and UOR (Fig. S17). In the

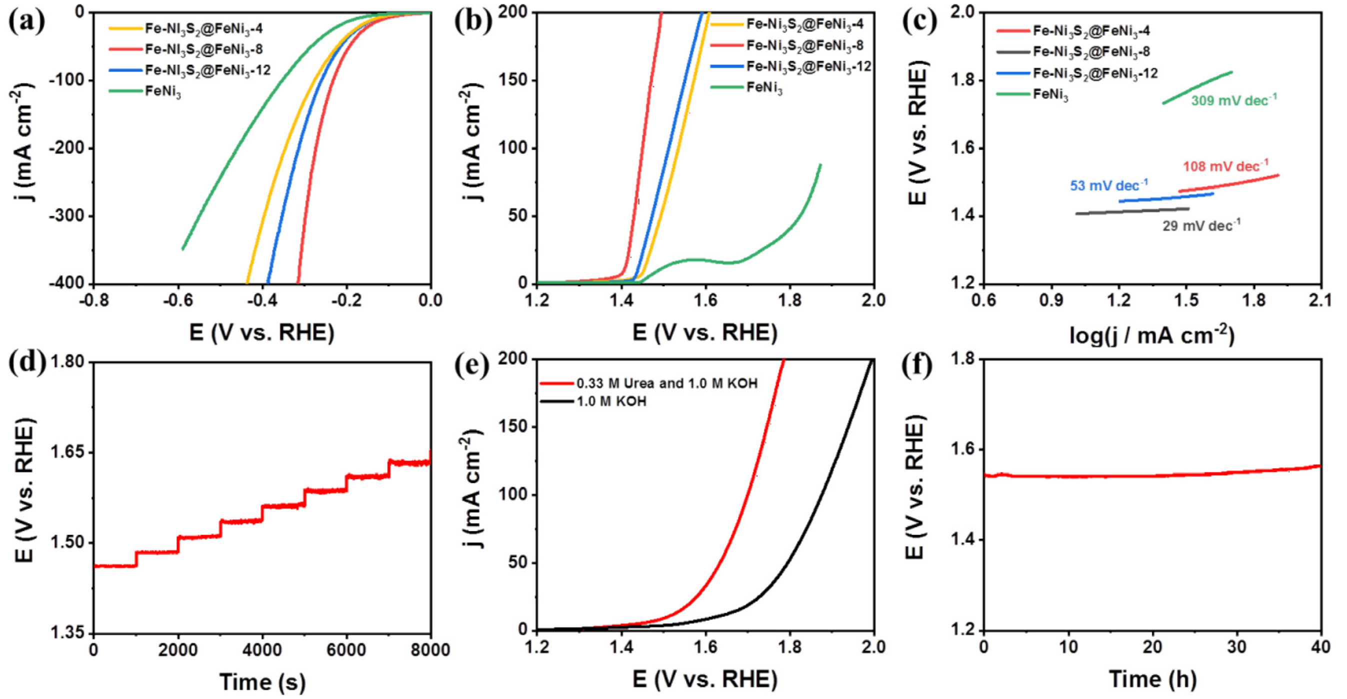

Fig. 7. (a) Electrochemical (a) HER and (b) UOR properties of the electrocatalysts in 0.33 M urea and 1.0 M KOH solution. Polarization curves (iR-corrected) at a scan rate of 5 mV s^{-1}. (c) Tafel plots of Fe-Ni_3S_2@$FeNi_3$-(4, 8, 12) and $FeNi_3$ for UOR. (d) Multi-current process of Fe-Ni_3S_2@$FeNi_3$-8. The current density started at 20 mA cm^{-2} and finished at 90 mA cm^{-2}, with an increment of 10 mA cm^{-2} every 1000 s without iR correction for UOR. (e) Polarization curves (without iR compensation) for water electrolysis of Fe-Ni_3S_2@$FeNi_3$-8‖ Fe-Ni_3S_2@$FeNi_3$-8 in a two-electrode configuration at a scan rate of 5 mVs^{-1} in 0.33 M urea and 1.0 M KOH solution, 1.0 M KOH solution. (f) Chronopotentiometric response curve of Fe-Ni_3S_2@$FeNi_3$-8‖Fe-Ni_3S_2@$FeNi_3$-8 at a current density of 10 mA cm^{-2} for 40 h. All experiments were carried out in 0.33 M Urea and 1.0 M KOH solution.

presence of urea, Fe-Ni_3S_2@$FeNi_3$-8 was assembled into a two-electrode system to test the catalytic performance of Fe-Ni_3S_2@$FeNi_3$-8 for whole urea electrolysis. Obviously, Fe-Ni_3S_2@$FeNi_3$-8 only requires 1.50 V to provide the current density of 10 mA cm^{-2} in the presence of urea, which is lower than that required in 1.0 M KOH solution (η_{10} = 1.59 V) (Fig. 7e). After testing, the catalytic activity of Pt/C‖RuO_2 (η_{10} = 1.53 V) is also inferior to that of Fe-Ni_3S_2@$FeNi_3$-8‖Fe-Ni_3S_2@$FeNi_3$-8 (Fig. S16c). In addition, after a long-term stability test of 40 h, it can be seen that Fe-Ni_3S_2@$FeNi_3$-8 has almost maintained its original activity (Fig. 7f). In addition, Fe-Ni_3S_2@$FeNi_3$-8 still maintains its original rod-like array structure, and Ni, Fe and S elements can still be detected from it (Fig. S18). After XRD characterization, it was found that the XRD peaks of Fe-Ni_3S_2@$FeNi_3$-8 remained basically intact after the multi-step chronoamperometry test (Fig. S16d).

The excellent catalytic activity of Fe-Ni_3S_2@$FeNi_3$-8 can be attributed to the following points: (1) The Fe-Ni_3S_2 nanorods are closely connected each other, which significantly contributes to the rapid transfer of electrons; (2) The regular rod-shaped array exposes a large number of active sites, thereby exhibits enhanced catalytic activity; (3) The doping of trace amount of Fe makes great contribution to the catalytical performance; (4) Fe-Ni_3S_2 is directly grown on the foam $FeNi_3$ with complete coverage, which can prevent corrosion of the 3D skeleton during the catalytic process, thereby prolonging the life time of the catalyst.

4. Conclusions

All in all, we have developed a Ni_3S_2 3D rod array structures doped with trace amount of Fe by a simple and quick one-step hydrothermal method, which are used as novel non-precious metal catalysts. The catalysts can be used as self-supporting electrodes with excellent catalytic activity for HER and OER in 1.0 M KOH solution. In addition, it also has excellent catalytic activity for HER in 0.5 M H_2SO_4 and 1.0 M PBS solution. The catalyst not only has an ultra-low overpotential but also excellent catalytic stability. The robust rod-like array structure not only exposes more active sites, but also stabilizes the performance of the catalyst. In addition, when Fe-Ni_3S_2@$FeNi_3$-8 is directly used as a bifunctional electrode in an alkaline electrolytic cell, it can reach the current density of 10 mA cm^{-2} with a potential of only 1.59 V and exhibits ultra-stable catalytic activity. In addition, in 0.33 M urea and 1.0 M KOH solution, a potential of only 1.40 V is required to achieve the current density of 10 mA cm^{-2}. After replacing the OER with a low-energy UOR, the reconstituted two-electrode system can provide the current density of 10 mA cm^{-2} with a potential of only 1.50 V. This work provides a quick and easy way to prepare a bifunctional catalyst for efficient overall water splitting.

Declaration of Competing Interest

The authors declare that they have no known competing financial interests or personal relationships that could have appeared to influence the work reported in this paper.

Acknowledgments

The authors acknowledge the National Natural Science Foundation of China (21805124), Natural Science Foundation of Shandong Province (ZR2018BEM020).

Appendix A. Supplementary data

Supplementary data to this article can be found online at https://doi.org/10.1016/j.cej.2020.125315.

References

[1] A.J. Bard, M.A. Fox, Artificial photosynthesis: solar splitting of water to hydrogen and oxygen, Acc. Chem. Res. 28 (1995) 141–145.

[2] J. Wang, W. Cui, Q. Liu, Z. Xing, A. Asiri, X. Sun, Recent Progress in Cobalt-Based Heterogeneous Catalysts for Electrochemical Water Splitting, Adv. Mater. 28 (2016) 215–230.

[3] J. Li, M. Yan, X. Zhou, Z. Huang, Z. Xia, C. Chang, Y. Ma, Y. Qu, Mechanistic Insights on Ternary $Ni_{2-x}Co_xP$ for Hydrogen Evolution and Their Hybrids with Graphene as Highly Efficient and Robust Catalysts for Overall Water Splitting, Adv. Funct. Mater. 26 (2016) 6785–6796.

[4] J.O.M. Bockris, T.N. Veziroglu, Estimates of the price of hydrogen as a medium for wind and solar sources, Int. J. Hydrogen Energy 32 (2007) 1605–1610.

[5] M.D. Symes, L. Cronin, Decoupling hydrogen and oxygen evolution during electrolytic water splitting using an electron-coupled-proton buffer, Nat. Chem. 5 (2013) 403.

[6] L. Trotochaud, J.K. Ranney, K.N. Williams, S.W. Boettcher, Solution-Cast Metal Oxide Thin Film Electrocatalysts for Oxygen Evolution, J. Am. Chem. Soc. 134 (2012) 17253–17261.

[7] Y. Lee, J. Suntivich, K.J. May, E.E. Perry, Y. Shao-Horn, Synthesis and activities of rutile IrO_2 and RuO_2 nanoparticles for oxygen evolution in acid and alkaline solutions, J. Phys. Chem. Lett. 3 (2012) 399–404.

[8] G. Chen, T.Y. Ma, Z. Liu, N. Li, Y. Su, K. Davey, S. Qiao, Efficient and Stable Bifunctional Electrocatalysts Ni/Ni_xM_y (M = P, S) for Overall Water Splitting, Adv. Funct. Mater. 26 (2016) 3314–3323.

[9] W. Zhu, X. Yue, W. Zhang, S. Yu, Y. Zhang, J. Wang, J. Wang, Nickel sulfide microsphere film on Ni foam as an efficient bifunctional electrocatalyst for overall water splitting, Chem. Commun. 52 (2016) 1486–1489.

[10] B. Chen, R. Li, G. Ma, X. Gou, Y. Zhu, Y. Xia, Cobalt sulfide/N, S codoped porous carbon core–shell nanocomposites as superior bifunctional electrocatalysts for oxygen reduction and evolution reactions, Nanoscale 7 (2015) 20674–20684.

[11] Y. Zheng, X. Wang, W. Zhao, X. Cao, J. Liu, Phytic acid-assisted synthesis of ultrafine $NiCo_2S_4$ nanoparticles immobilized on reduced graphene oxide as high-performance electrode for hybrid supercapacitors, Chem. Eng. J. 333 (2018) 603–612.

[12] A. Zhang, A. Li, W. Zhao, G. Yan, B. Liu, M. Liu, M. Li, B. Huo, J. Liu, An efficient and self-guided chemo-photothermal drug loading system based on copolymer and transferrin decorated MoS_2 nanodots for dually controlled drug release, Chem. Eng. J. 342 (2018) 120–132.

[13] B. Dong, X. Zhao, G.Q. Han, X. Li, X. Shang, Y.R. Liu, W.-H. Hu, Y.M. Chai, H. Zhao, C.G. Liu, Two-step synthesis of binary Ni–Fe sulfides supported on nickel foam as highly efficient electrocatalysts for the oxygen evolution reaction, J. Mater. Chem. A 4 (2016) 13499–13508.

[14] K.L. Yan, J.F. Qin, Z.Z. Liu, B. Dong, J.Q. Chi, W.K. Gao, J.H. Lin, Y.M. Chai, C.G. Liu, Organic-inorganic hybrids-directed ternary NiFeMoS anemone-like nanorods with scaly surface supported on nickel foam for efficient overall water splitting, Chem. Eng. J. 334 (2018) 922–931.

[15] Y.M. Chai, X.Y. Zhang, J.H. Lin, J.F. Qin, Z.Z. Liu, J.Y. Xie, B.Y. Guo, Z. Yang, B. Dong, Three-dimensional VO_x/NiS/NF nanosheets as efficient electrocatalyst for oxygen evolution reaction, Int. J. Hydrogen Energy 44 (2019) 10156–10162.

[16] X. Shang, B. Dong, Y.M. Chai, C.G. Liu, In-situ electrochemical activation designed hybrid electrocatalysts for water electrolysis, Sci. Bull. 63 (2018) 853–876.

[17] Y. Tan, H. Wang, P. Liu, Y. Shen, C. Cheng, A. Hirata, T. Fujita, Z. Tang, M. Chen, Versatile nanoporous bimetallic phosphides towards electrochemical water splitting, Energy Environ. Sci. 9 (2016) 2257–2261.

[18] C. Ray, S.C. Lee, B. Jin, A. Kundu, J.H. Park, S.C. Jun, Stacked Porous Iron-Doped Nickel Cobalt Phosphide Nanoparticle: An Efficient and Stable Water Splitting Electrocatalyst, ACS Sustain. Chem. Eng. 6 (2018) 6146–6156.

[19] X. Cao, D. Jia, D. Li, L. Cui, J. Liu, One-step co-electrodeposition of hierarchical radial Ni_xP nanospheres on Ni foam as highly active flexible electrodes for hydrogen evolution reaction and supercapacitor, Chem. Eng. J. 348 (2018) 310–318.

[20] Z. Pu, Y. Luo, A.M. Asiri, X. Sun, Efficient Electrochemical Water Splitting Catalyzed by Electrodeposited Nickel Diselenide Nanoparticles Based Film, ACS Appl. Mater. Interfaces 8 (2016) 4718–4723.

[21] X. Xu, F. Song, X. Hu, A nickel iron diselenide-derived efficient oxygen-evolution catalyst, Nat. Commun. 7 (2016) 12324.

[22] X. Zhou, Z. Xia, Z. Tian, Y. Ma, Y. Qu, Ultrathin porous Co_3O_4 nanoplates as highly efficient oxygen evolution catalysts, J. Mater. Chem. A 3 (2015) 8107–8114.

[23] G.S. Hutchings, Y. Zhang, J. Li, B.T. Yonemoto, X. Zhou, K. Zhu, F. Jiao, In Situ Formation of Cobalt Oxide Nanocubanes as Efficient Oxygen Evolution Catalysts, J. Am. Chem. Soc. 137 (2015) 4223–4229.

[24] M. Gong, W. Zhou, M. Tsai, J. Zhou, M. Guan, M. Lin, B. Zhang, Y. Hu, D. Wang, J. Yang, S.J. Pennycook, B. Hwang, H. Dai, Nanoscale nickel oxide/nickel heterostructures for active hydrogen evolution electrocatalysis, Nat. Commun. 5 (2014) 4695.

[25] J. Suntivich, K.J. May, H.A. Gasteiger, J.B. Goodenough, Y. Shaohorn, A perovskite oxide optimized for oxygen evolution catalysis from molecular orbital principles, Science 334 (2011) 1383–1385.

[26] X. Xu, Y. Chen, W. Zhou, Z. Zhu, C. Su, M. Liu, Z. Shao, A Perovskite Electrocatalyst for Efficient Hydrogen Evolution Reaction, Adv. Mater. 28 (2016) 6442–6448.

[27] M. Gao, W. Sheng, Z. Zhuang, Q. Fang, S. Gu, J. Jiang, Y. Yan, Efficient water oxidation using nanostructured α-nickel-hydroxide as an electrocatalyst, J. Am. Chem. Soc. 136 (2014) 7077–7084.

[28] S.L. Candelaria, N.M. Bedford, T.J. Woehl, N.S. Rentz, A.R. Showalter, S. Pylypenko, B.A. Bunker, S. Lee, B. Reinhart, Y. Ren, S.P. Ertem, E.B. Coughlin, N.A. Sather, J.L. Horan, A.M. Herring, L.F. Greenlee, Multi-Component Fe–Ni Hydroxide Nanocatalyst for Oxygen Evolution and Methanol Oxidation Reactions under Alkaline Conditions, ACS Catal. 7 (2017) 365–379.

[29] X. Xu, Y. Zhong, Z. Shao, Double perovskites in catalysis, electrocatalysis, and photo (electro)catalysis, Trends in Chemistry 1 (2019) 410–424.

[30] J. Ren, Z. Yuan, Hierarchical nickel sulfide nanosheets directly grown on ni foam: a stable and efficient electrocatalyst for water reduction and oxidation in alkaline medium, ACS Sustain. Chem. Eng. 5 (2017) 7203–7210.

[31] Q. Ma, C. Hu, K. Liu, S.F. Hung, D. Ou, H.M. Chen, G. Fu, N. Zheng, Identifying the electrocatalytic sites of nickel disulfide in alkaline hydrogen evolution reaction, Nano Energy 41 (2017) 148–153.

[32] J. Zhang, T. Wang, D. Pohl, B. Rellinghaus, R. Dong, S. Liu, X. Zhuang, X. Feng, Interface engineering of MoS_2/Ni_3S_2 heterostructures for highly enhanced electrochemical overall-water-splitting activity, Angew. Chem. Int. Ed. 55 (2016) 6702–6707.

[33] J. Yan, H. Wu, P. li, H. Chen, R. Jiang, S. Liu, Fe(iii) doped NiS2 nanosheet: a highly efficient and low-cost hydrogen evolution catalyst, J. Mater. Chem. A 5 (2017) 10173-10181.

[34] W. Zhang, D. Li, L. Zhang, X. She, D. Yang, NiFe-based nanostructures on nickel foam as highly efficiently electrocatalysts for oxygen and hydrogen evolution reactions, J. Energy Chem. 39 (2019) 39–53.

[35] Y. Hua, Q. Xu, Y. Hu, H. Jiang, C. Li, Interface-strengthened CoP nanosheet array with Co_2P nanoparticles as efficient electrocatalysts for overall water splitting, J. Energy Chem. 37 (2019) 1–6.

[36] B. Wang, C. Tang, H.F. Wang, B.Q. Li, X. Cui, Q. Zhang, J.S. Methods, Anion-Regulated Hydroxysulfide Monoliths as OER/ORR/HER Electrocatalysts and their Applications in Self-Powered Electrochemical Water Splitting, Small 1800055 (2018).

[37] W. Zhang, G. Chen, J. Zhao, J. Liang, G. Liu, B. Ji, L. Sun, Fe-doped $CoNi_{0.5}P$ Hierarchical Arrays as Efficient Bifunctional Electrocatalysts for Overall Water Splitting: Evolution of Morphology and Coordination of Catalytic Performance, ChemistrySelect 4 (2019) 6744–6752.

[38] N. Xiong, S. Wang, Y. Xie, Q. Feng, X. Wang, M. Li, Z. Xu, W. Zhou, K. Pan, Multifunctional $(Fe_{0.5}Ni_{0.5})S_2$ nanocrystal catalysts with high catalytic activities for reduction of I^{3-} and electrochemical water splitting, Res. Chem. Intermed. 44 (2018) 4307–4322.

[39] L.L. Feng, G. Yu, Y. Wu, G.D. Li, H. Li, Y. Sun, T. Asefa, W. Chen, X. Zou, High-Index Faceted Ni_3S_2 Nanosheet Arrays as Highly Active and Ultrastable Electrocatalysts for Water Splitting, J. Am. Chem. Soc. 137 (2015) 14023–14026.

[40] L. Li, C. Sun, B. Shang, Q. Li, J. Lei, N. Li, F. Pan, Tailoring the facets of Ni_3S_2 as a bifunctional electrocatalyst for high-performance overall water-splitting, J. Mater. Chem. A 7 (2019) 18003–18011.

[41] C. Tang, R. Zhang, W. Lu, Z. Wang, D. Liu, S. Hao, G. Du, A.M. Asiri, X. Sun, Energy-Saving Electrolytic Hydrogen Generation: Ni2P Nanoarray as a High-Performance Non-Noble-Metal Electrocatalyst, Angew. Chem. Int. Ed. 56 (2017) 842–846.

[42] T. Liu, D. Liu, F. Qu, D. Wang, L. Zhang, R. Ge, S. Hao, Y. Ma, G. Du, A.M. Asiri, L. Chen, X. Sun, Enhanced Electrocatalysis for Energy-Efficient Hydrogen Production over CoP Catalyst with Nonelectroactive Zn as a Promoter, Adv. Eng. Inf. 7 (2017) 1700020.

[43] W. Yan, D. Wang, L.A. Diaz, G.G. Botte, Nickel nanowires as effective catalysts for urea electro-oxidation, Electrochim. Acta 134 (2014) 266–271.

[44] D. Liu, T. Liu, L. Zhang, F. Qu, G. Du, A.M. Asiri, X. Sun, High-performance urea electrolysis towards less energy-intensive electrochemical hydrogen production using a bifunctional catalyst electrode, J. Mater. Chem. A 5 (2017) 3208–3213.

[45] A.N. Rollinson, J. Jones, V. Dupont, M.V. Twigg, Urea as a hydrogen carrier: a perspective on its potential for safe, sustainable and long-term energy supply, Energy Environ. Sci. 4 (2011) 1216–1224.

[46] R. Ding, L. Qi, M. Jia, H. Wang, Facile synthesis of mesoporous spinel $NiCo_2O_4$ nanostructures as highly efficient electrocatalysts for urea electro-oxidation, Nanoscale 6 (2014) 1369–1376.

[47] B. Yang, L. Yu, Q. Liu, J. Liu, W. Yang, H. Zhang, F. Wang, S. Hu, Y. Yuan, J. Wang, The growth and assembly of the multidimensional hierarchical Ni_3S_2 for aqueous asymmetric supercapacitors, CrystEngComm 17 (2015) 4495–4501.

[48] Z. Xing, Q. Liu, A.M. Asiri, X. Sun, Closely Interconnected Network of Molybdenum Phosphide Nanoparticles: A Highly Efficient Electrocatalyst for Generating Hydrogen from Water, Adv. Mater. 26 (2014) 5702–5707.

[49] W. Zhou, X.-J. Wu, X. Cao, X. Huang, C. Tan, J. Tian, H. Liu, J. Wang, H. Zhang, Ni_3S_2 nanorods/Ni foam composite electrode with low overpotential for electrocatalytic oxygen evolution, Energy Environ. Sci. 6 (2013) 2921–2924.

[50] M.C. Biesinger, B.P. Payne, L.W.M. Lau, A. Gerson, R.S.C. Smart, X-ray photoelectron spectroscopic chemical state quantification of mixed nickel metal, oxide and hydroxide systems, Surf. Interface Anal. 41 (2009) 324–332.

[51] C. Wang, R. Wang, Y. Peng, J. Chen, J. Li, Iron tungsten mixed composite as a robust oxygen evolution electrocatalyst, Chem. Commun. 55 (2019) 10944–10947.

[52] X. Hu, Q. Zhou, P. Cheng, S. Su, X. Wang, X. Gao, G. Zhou, Z. Zhang, J. Liu, Nickel-iron selenide polyhedral nanocrystal with optimized surface morphology as a high-performance bifunctional electrocatalyst for overall water splitting, Appl. Surf. Sci. 488 (2019) 326–334.

[53] C. Dueso, M.T. Izquierdo, F. García-Labiano, L.F. de Diego, A. Abad, P. Gayán, J. Adánez, Effect of H_2S on the behaviour of an impregnated NiO-based oxygen-carrier for chemical-looping combustion (CLC), Appl. Catal., B 126 (2012) 186–199.

[54] A.G. Schaufuß, H.W. Nesbitt, I. Kartio, K. Laajalehto, G.M. Bancroft, R. Szargan, Incipient oxidation of fractured pyrite surfaces in air, J. Electron. Spectrosc. Relat. Phenom. 96 (1998) 69–82.

[55] W. Zhu, L. Liu, Z. Yue, W. Zhang, X. Yue, J. Wang, S. Yu, L. Wang, J. Wang, Au promoted nickel-iron layered double hydroxide nanoarrays: a modular catalyst

enabling high-performance oxygen evolution, ACS Appl. Mater. Interfaces 9 (2017) 19807–19814.
[56] M.B. Stevens, L.J. Enman, A.S. Batchellor, M.R. Cosby, A.E. Vise, C.D.M. Trang, S.W. Boettcher, Measurement techniques for the study of thin film heterogeneous water oxidation electrocatalysts, Chem. Mater. 29 (2017) 120–140.
[57] L. Trotochaud, S.L. Young, J.K. Ranney, S.W. Boettcher, Nickel-iron oxyhydroxide oxygen-evolution electrocatalysts: the role of intentional and incidental iron incorporation, J. Am. Chem. Soc. 136 (2014) 6744–6753.
[58] A. Grimaud, W.T. Hong, Y. Shao Horn, J.M. Tarascon, Anionic redox processes for electrochemical devices, Nat. Mater. 15 (2016) 121–126.
[59] M.W. Louie, A.T. Bell, An investigation of thin-film ni–fe oxide catalysts for the electrochemical evolution of oxygen, J. Am. Chem. Soc. 135 (2013) 12329–12337.
[60] B. Song, K. Li, Y. Yin, T. Wu, L. Dang, M. Cabán Acevedo, J. Han, T. Gao, X. Wang, Z. Zhang, J.R. Schmidt, P. Xu, S. Jin, Tuning Mixed Nickel Iron Phosphosulfide Nanosheet Electrocatalysts for Enhanced Hydrogen and Oxygen, Evolution, ACS Catal. 7 (2017) 8549–8557.
[61] P. Li, X. Duan, Y. Kuang, Y. Li, G. Zhang, W. Liu, X. Sun, Tuning Electronic Structure of NiFe Layered Double Hydroxides with Vanadium Doping toward High Efficient Electrocatalytic Water Oxidation, Adv. Energy Mater. 8 (2018) 1703341.
[62] Y. Li, L. Zhang, X. Xiang, D. Yan, F. Li, Engineering of ZnCo-layered double hydroxide nanowalls toward high-efficiency electrochemical water oxidation, J. Mater. Chem. A 2 (2014) 13250–13258.
[63] B.C.M. Martindale, E. Reisner, Bi-Functional Iron-Only Electrodes for Efficient Water Splitting with Enhanced Stability through In Situ Electrochemical Regeneration, Adv. Energy Mater. 6 (2016) 1502095.
[64] Y. Liu, S. Jiang, S. Li, L. Zhou, Z. Li, J. Li, M. Shao, Interface engineering of (Ni, Fe) S_2@MoS_2 heterostructures for synergetic electrochemical water splitting, Appl. Catal., B 247 (2019) 107–114.
[65] J. Yu, F. Ma, Y. Du, P. Wang, C. Xu, L. Zhen, In Situ Growth of Sn-Doped Ni_3S_2 Nanosheets on Ni Foam as High-Performance Electrocatalyst for Hydrogen Evolution Reaction, ChemElectroChem 4 (2017) 594–600.
[66] J. Jiang, S. Lu, H. Gao, X. Zhang, H. Yu, Ternary $FeNiS_2$ ultrathin nanosheets as an electrocatalyst for both oxygen evolution and reduction reactions, Nano Energy 27 (2016) 526–534.
[67] L. Lin, Q. Fu, Y. Han, J. Wang, X. Zhang, Y. Zhang, C. Hu, Z. Liu, Y. Sui, X. Wang, Fe doped skutterudite-type CoP_3 nanoneedles as efficient electrocatalysts for hydrogen and oxygen evolution in alkaline media, J. Alloys Compd. 808 (2019) 151767.
[68] Y. Hou, M. Qiu, G. Nam, M.G. Kim, T. Zhang, K. Liu, X. Zhuang, J. Cho, C. Yuan, X. Feng, Integrated Hierarchical Cobalt Sulfide/Nickel Selenide Hybrid Nanosheets as an Efficient Three-dimensional Electrode for Electrochemical and Photoelectrochemical Water Splitting, Nano Lett. 17 (2017) 4202–4209.
[69] A. Sivanantham, P. Ganesan, S. Shanmugam, Hierarchical $NiCo_2S_4$ nanowire arrays supported on ni foam: An efficient and durable bifunctional electrocatalyst for oxygen and hydrogen evolution reactions, Adv. Funct. Mater. 26 (2016) 4661–4672.
[70] Y. Yang, H. Yao, Z. Yu, S.M. Islam, H. He, M. Yuan, Y. Yue, K. Xu, W. Hao, G. Sun, H. Li, S. Ma, P. Zapol, M.G. Kanatzidis, Hierarchical Nanoassembly of MoS_2/Co_9S_8/Ni_3S_2/Ni as a Highly Efficient Electrocatalyst for Overall Water Splitting in a Wide pH Range, J. Am. Chem. Soc. 141 (2019) 10417–10430.